Quantitative analysis of fluvial paleohydraulics and intra-channel belt stratal preservation: lower Wasatch Formation, Utah, USA

Jesse Pisel[1], David Pyles[2]

[1]Wyoming State Geological Survey, P.O. Box 1347, Laramie WY; Email: jessepisel@gmail.com

[2]EOG Resources Inc, 600 17th St. Denver CO

ABSTRACT

This article uses measurements from five fluvial channel belts of the Paleocene lower Wasatch Formation to quantitatively document the transience or persistence of flow velocities recorded in stratigraphy at the bedset scale. We use facies proportions and sedimentary structures coupled with a paleoflow velocity workflow to calculate the mean flow velocity for each bedset. Flow velocity measurements were analyzed using a lattice approach that documents either persistence or transience of mean flow velocities, which, in turn was combined with facies trends to infer perennial and ephemeral flow conditions during the deposition of the channel belt. All five channel belts have significant spatial dependence of mean flow velocities. Based on short-range spatial dependence, we infer perennial flow conditions in both laterally and downstream-accreting channel belts, and ephemeral flow conditions in two downstream-accreting channel belts. The remaining channel belt only has short-range spatial dependence as intra channel-belt erosion has completely destroyed any intermediate and long-range flow velocity dependence within the channel belt. Furthermore, we document that intra channel-belt stratal preservation comes at the expense of basin-scale stratal preservation, meaning high channel migration rates destroy basin-scale architecture (stacking patterns) by channel scouring while preserving intra channel-belt morphodynamics at the bedset scale.

INTRODUCTION

External forcing (allogenic) mechanisms such as changes in tectonic uplift, subsidence rates, climate fluctuations, and eustasy have been documented in fluvial stratigraphy and simulated in forward numerical models (Foreman et al., 2012; Allen et al., 2013; Allen et al., 2014). Time series methods have been used to document allogenic signals, including spectral analysis of Fourier and wavelet transforms, as well as autocorrelation functions (Prokoph and Agterberg, 1999; Prokoph and Bilali, 2008; Jerolmack and Paola, 2009). However, recent research documents that internal (autogenic) mechanisms act as a non-linear filter that can destroy allogenic signals if the amplitude and period of the external signal is less than the noise of the sediment transport system (Jerolmack and Paola, 2009). Recognizing allogenic signals in stratigraphy is important for predicting how fluvial systems respond to tectonic, climatic, and eustatic changes. Allogenic signals have been documented at the basin scale (100-1,000 m scale thickness), however few studies have concentrated on the channel-belt and bar scale (1-100 m thick) (e.g. Allen et al., 2014). In this study we use the term bedset, which is a hierarchical term, used to describe stratigraphy composed of smaller beds, is genetically related, similar in areal extent and time span of deposition (Ford and Pyles, 2014), and is comparable to an active barform migrating through an active channel.

Two end-member channel-belt types have been interpreted to document short term (yearly to decadal) climatic signals, perennial and ephemeral. Perennial channel belts are interpreted to document persistent flow conditions, with annual to decadal fluctuations related to seasonality in sediment and water flux (Meinzer, 1923; Fielding et al., 2009). Ephemeral channel belts document transient flow conditions between wet and dry periods (McKee et al., 1967; North and Taylor, 1996). Despite differences in flow conditions and bedforms associated with the two channel belt types, documenting persistence or transience of flow conditions on a decadal to 100 year timescale within ancient fluvial channel belts remains challenging. This study uses cross sections, measured sections, grain-size distributions, lithofacies, and bedset bounding surfaces to document allogenic climate signals within fluvial channel belts.

GEOLOGIC SETTING

The lower Wasatch Formation of the Uinta Basin in eastern Utah contains world class exposures of a low net-sand content fluvial system. The Uinta Basin is a longitudinally asymmetric foreland basin located in northeastern and central Utah (Figure 1A). From the Paleocene through Eocene, flexurally induced subsidence provided accommodation for deposition of the Green River and Wasatch Formations (Figure 1A) (Osmond, 1964). Lacustrine sediments deposited in the center of the basin were surrounded by deltaic and fluvial strata of the Green River and Wasatch Formations; signifying internal drainage (Picard, 1955; Keighley et al., 2002). Paleocurrent directions in the southern outcrops of the Wasatch Formation document fluvial systems flowing north and northeast towards the center of the basin (Ford and Pyles, 2014, Pisel et al., 2018) (see paleocurrent rose diagram in Figure 1B). Climatically, the lower Wasatch Formation is interpreted to have been deposited during global hot house conditions (Sewall and Sloan, 2006). Basin-scale studies in the adjacent Piceance basin document hundred thousand year changes in channel belt dimensions and sedimentary structures attributed to climatic fluctuations at the Paleocene-Eocene Thermal Maximum (Foreman et al., 2012).

DATASET AND METHODS

An exceptionally well exposed, strike-oriented outcrop of the lower Wasatch Formation is used to address the goals of this study (Figure 1B). The outcrop is located along the southern margin of the Uinta basin, just west of the modern day Green River (39.352 N, 110.063 W), and is 5 km wide by 300 m thick. The outcrop contains 274 fluvial channel belts, all of which are exceptionally well exposed and accessible. Five channel belts were analyzed in detail. They represent the range of architectural variability in the outcrop and span a range of varying numbers of stories and accretion styles. Using the hierarchical approach of Ford and Pyles (2014) the 5 channel belts were characterized on the basis of bar migration direction as follows (Figure 2): (Channel Belt 1) laterally-accreting multi story, (Channel Belt 2) downstream and laterally accreting multi story, (Channel Belt 3) downstream-accreting single story, (Channel Belt 4) downstream-accreting multi story, (Channel Belt 5) laterally-accreting with erosionally based fine-grained fill multi story, respectively (Figure 2).

The following data were collected to address the goals of this study: (1) decimeter-resolution measured sections that qualitatively documents grain-size distributions, sorting, rounding, physical and biogenic sedimentary structures, bedset, story, and element boundaries; (2) high-resolution photo panels; (3) paleocurrent orientations collected from flutes, ripples, cross-strata, channel-belt margin orientations; and (4) laser range finding measurements of element, story, and bar form widths and thicknesses. These data were used to generate further information about the channel belts using the following workflow. First, grain size distributions were calculated from measured sections where grain size was optically measured using hand lens and grain size card. Median grain size (D_{50}) and maximum grain size (D_{90}) are calculated from the distributions for each channel belt (Figure 3A). Cross-sections of the channel belts were created by tracing bedset boundaries in the photo panels and combined with measured sections to constrain grain size and facies type for each bedset. Additionally, measured bar-form heights were used to constrain flow depths for bedsets as bar forms scale to flow depth (Figure 3C).

From the field data we calculate the mean slope from all 5 channel belts using the paleoslope reconstruction suspension methods of Lynds et al. (2014). To calculate paleoslope using this method we first we calculate the settling velocity of the coarsest grains in suspension ($w_{s(dmaxs)}$) using the equation from Ferguson and Church (2004):

$$w_{s(Dmaxs)} = \frac{gRD_{90}{}^{2}}{18\nu+(0.75CgRD_{90}{}^{3})^{1/2}} \quad (1)$$

where g is the acceleration of gravity, R is the specific gravity of the particle in the water, D_{90} is the maximum grain size, ν is the kinematic viscosity of the fluid, and C is a constant equal to 1 for typical sand grains. Next we calculate z_0 which is the height at which the velocity goes to zero. To calculate z_0 we use the assumption of Lynds et al. (2014) based on Wiberg and Rubin (1989) that $z_0 = 0.056b$ and b is approximately two times the median bedload grain size $b \approx 2.0D_{50b}$ which we approximate by substituting D_{90} for D_{50b}. Using z_0 we then calculate the ratio of total boundary stress to skin-friction shear stress:

$$F = 1 + \frac{C_d}{2\kappa^2}\frac{h_d}{\lambda}\left[\ln\left[\frac{h_d}{z_0}\right] - 1\right]^2 \quad (2)$$

where C_d is an empirically determined drag coefficient (0.21), κ is von Kármán's constant, h_d is 0.3 times flow depth (0.3H), and the dune height-to-length ratio h_d/λ is 0.063 (Lynds et al., 2014). Now that we have calculated $w_{s(Dmaxs)}$ and F we can calculate paleoslope for the lower Wasatch Formation using the following from Lynds et al., (2014):

$$S = \frac{F(w_{s(Dmaxs)})^2}{g\langle H\rangle} \quad (3)$$

where S is slope, F is the ratio of total boundary shear stress to skin-friction shear stress, $w_{s(dmaxs)}$ is the settling velocity of the coarsest grain in suspension, g is gravity, and H is flow depth. The limitations of paleoslope reconstructions have been discussed by Trampush et al. (2014), and

Lynds et al. (2014), so now we will now cover the potential for error and how it propagates through this system of equations in our slope calculations.

We use Sobol indices to quantitatively understand the sensitivity of the paleoslope estimates. Sobol indices are a normalized decomposition of variance that can be attributed to specific inputs to the model. As Sobol index values for a single input approach 1 they have more fractional variance associated with that variable (Sobol, 2001; Saltelli, 2002; Saltelli et al., 2010). Meaning that the larger the value, the more influence a particular variable has in the system. We ran 30,000 simulations of paleoslope estimates to calculate Sobol indices for each source of error in the calculation. For 10,000 simulations we varied D_{90} by $\pm 1\phi$ grain size larger and smaller than our observed values. For 10,000 simulations we varied D_{50} by $\pm 1\phi$ grain size larger and smaller than our observed values. And finally for 10,000 simulations we varied flow depth (H) by ±35% of the average flow depth of channel belts in the lower Wasatch Formation (9.1±3.185 m). The resulting first order Sobol indices are as follows 0.8982 (D_{90}), 0.0126 (D_{50}), 0.0259 (H). These results document that the maximum grain size and flow depth have first order controls on paleoslope. Total order Sobol indices are 0.9634 (D_{90}), 0.0126 (D_{50}), and 0.0661 (H) respectively, and document weak higher order interactions between the three variables, of which none are significant. Again, the sensitivity analysis was based on an assumed error of $\pm 1\phi$ grain size and 90% variance in flow depth.

Now that we have quantitatively documented which variables have first and second order controls, we can calculate paleoslope and associated uncertainty. We use one standard deviation as our uncertainty bounds based on a grain size error of $\pm 1\phi$ for both D_{90} and D_{50}. This uncertainty is based on the assumption that our grain size measurements are within 1ϕ of the mean grain size. We think that this assumption is reasonable as it would be comparable to mistaking coarse sand for fine sand. Additionally, we assume that our flow depth is within 35% (±3.185 m) of the mean channel-belt flow depth (9.1 m) for all measured channel belts in the lower Wasatch (Pisel et al., 2018). From these assumed sources of error, we calculate the paleoslope of the lower Wasatch Formation to be 2.8×10^{-3} with a maximum of 5.4×10^{-3} and a minimum of 1.6×10^{-4}. The mean and lower limits are well within the reasonable bounds discussed by Trampush (2014) while the upper slope estimate is on the edge of what they consider reasonable. Nevertheless, this gives us a place to further investigate paleoflows within the lower Wasatch Formation.

Using the mean paleoslope (2.8×10^{-3}) and flow depth measurements for each barform (Figure 3C) we calculate the bed shear stress using the depth-slope product (Leopold et al., 1964):

$$\tau_b = \rho g H S \tag{4}$$

where ρ is the density of the fluid, *g* is gravitational acceleration, *H* is flow depth, and *S* is slope. The flow depth is constrained by the amount of relief on the barforms, as they scale to the water surface, and are the most accurate measure of paleo-flowdepth. Next, we substitute in bed shear stress (equation 3) to calculate the shear velocity (Shields, 1936):

$$u_* = \sqrt{\frac{\tau_b}{\rho}} \tag{5}$$

where τ_b is the bed shear stress and ρ is the fluid density. Finally, from the shear velocity (equation 4) we calculate the average velocity using the Law of the Wall (von Kármán, 1930):

$$u = \frac{u_*}{k}\left(ln\frac{z}{z_0}\right) \tag{6}$$

where z is the height of the velocity measurement, z_0 is the level at which the velocity goes to zero, u_* is the shear velocity, and k is von Kármán's constant. In this study we define z as 6/10ths the height of flow depth to calculate an average flow velocity. Furthermore, we define z_0 as we did during the previous slope calculations.

We further investigate error in our flow velocity calculations using Monte Carlo simulations to explore the distributions of potential flow velocities in the lower Wasatch Formation. Specifically we assume that the error in the maximum grain size, mean grain size, flow depth, and slope is normally distributed, centered on our field measured values, and that the standard deviations are the same as those used in the sensitivity analysis. Given these assumptions, the simulations proceed as follows: (1) select a bedset in the channel belt, (2) for the selected bedset calculate the paleoflow velocity distribution from the mean paleoflow velocity and its standard deviation, (3) randomly choose a velocity value from the velocity distribution for the bedset, (4) select the next bedset and repeat steps 1-3, (5) repeat this process 99 times for each channel belt before moving to the next channel belt and repeating steps 1-5. This builds a robust dataset with 35,900 data points for flow velocity and flow depth.

Next we visualize how the uncertainty in flow velocity changes with flow depth as a 2D kernel density estimate (Figure 4). Note that as flow depth increases, the variance in the flow velocity increases as well. We attribute this to the increase of variance in the slope estimate as flow depth increases. This is exactly what Trampush et al. (2014) discuss, that the error in flow depth estimates propagates through to the slope estimate. Here we document that flow depth uncertainty also propagates through to velocity calculations as well. Figure 4 documents the range of flow velocities that we generated from the Monte Carlo simulations for the channel belts in the lower Wasatch. Areas of higher density (lighter colors) infer a higher confidence in the calculation. Now that we have discussed how we calculate paleoflow velocities and sources of error within the systems of equations we will further discuss the analytical methods we used to spatially evaluate the data.

Spatial persistence and transience of mean flow velocity were quantified using spatial statistics and lattice methods. Lattice data are discrete, with each region represented by an average of the data. In this study we define regions by bedsets, and assign the mean-flow velocity to each. We define spatial neighborhoods for each bedset using row standardized weights, meaning that bedsets in contact with one another (linked) are spatially related. Beyond adjacent bedsets, we evaluated spatial autocorrelation of mean flow velocity at increasing, non-adjacent bedset lags using Moran's *I*. Bedset lag spatial autocorrelation simply increases the neighborhood structure to include beds that are not directly in contact with one another which documents long-range spatial trends. Spatial autocorrelation, which is the cross-correlation of a region with its neighbors, is calculated using Moran's *I*:

$$I = \frac{n}{\sum_{i=1}^{n}\sum_{j=1}^{n} w_{ij}} \frac{\sum_{i=1}^{n}\sum_{j=1}^{n} w_{ij}(y_i - \bar{y})(y_j - \bar{y})}{\sum_{i=1}^{n}(y_i - \bar{y})^2} \tag{7}$$

where y_i is the *i*-th observation, y_j is the *j*-th observation $\bar{y}$ is the global mean flow velocity and W_{ij} is the spatial weight of the link between regions *i* and *j* defined above using row standardized binary weights (Moran, 1950). The expected value of Moran's *I* under the null hypothesis of no spatial dependence is:

$$E(I) = \frac{-1}{N-1} \tag{8}$$

where *N* is the number of locations. To test for spatial autocorrelation using Moran's *I*, we use Monte Carlo simulations. In this test, 99 Monte Carlo simulations were run for each channel belt. Values for each region are randomly reassigned to a new region and Moran's *I* is calculated for each simulation. Calculated Moran's I is compared to the distribution of Moran's I from the Monte Carlo simulations. If the observed value of I is outside the distribution generated from the simulations ($p<0.05$), there is significant evidence for spatial autocorrelation. Moran's I ranges from -1 to 1, where negative values document negative correlation (transience), and positive values document positive correlation (persistence) and values near 0 document spatial independence.

RESULTS

Velocities

All five channel belts document increasing mean flow velocity with increasing flow depth as we expect given equation 5. In all five channel belts, a majority of the calculated variance stems from uncertainty in slope estimates. A slope of $2.8\text{x}10^{-3} \pm 2.5\text{x}10^{-3}$ results in the following mean flow velocities in meters per second: Channel Belt 1 0.55±0.29, Channel Belt 2 0.20±0.11, Channel Belt 3 0.28±0.14, Channel Belt 4 0.40±0.21, and Channel Belt 5 0.45±0.23. If we exclude the slope variance and only use flow depth and grain size variance for the velocity calculations, our standard deviation is half of what we calculate with the slope variance (Table 1). From the average flow velocities for each bedset, we calculate the spatial autocorrelation (Moran's I) for an increasing numbers of bedset lags.

Moran's *I*

For a bedset lag of 1, all five characters belts have documented positive spatial autocorrelation (or similarity) of mean flow velocity using Moran's I (Figure 5a). As we increase the region neighborhoods, or distance between bedsets, we document positive spatial autocorrelation up to 2 bedset lags for all the channel belts (Figure 5a). Meaning the mean flow velocities in all the channel belts are locally similar from bedset to bedset both vertically and laterally. Channel Belts 3 and 4 have positive spatial correlation at bedset lags of 3, while the mean flow velocity for Channel Belts 1, 2, and 5 is spatially independent and remains that way through 4 bedset lags. At bedset lags of 5 and 6, Channel Belts 1-4 have negative spatial autocorrelation of mean flow velocity (Figure 5b-e). This means mean flow velocities in intermediate bedsets, both vertically and laterally, are dissimilar. Channel Belt 5 has no correlation for any bedset lags higher than 2 (Figure 5f), meaning that mean flow velocities for all bedsets are spatially independent or different.

In all 5 channel belts the diagnostic sedimentary structures associated with high and low flow regimes coupled with facies proportions provide further information into the meaning of the Moran's *I* results. Specifically, spatial persistence of flow velocity, low facies diversity, and low flow regime associated facies are interpreted to be characteristic of perennial deposits. In contrast, spatial transience of flow velocity, high facies diversity, and high flow regime associated facies are interpreted to be characteristic of ephemeral deposits.

We interpret the short-range, positive autocorrelation, facies, and bar migration orientation in Channel Belts 1 and 5 to collectively record short term stasis in flow velocity. Both of these channel belts migrated solely laterally, which is interpreted to have preserved the depositional processes. From the facies proportions, we interpret Channel Belt 5 to document ephemeral deposits, as the facies record high flow regime conditions within the channel belt. Additionally in Channel Belt 5 we interpret that the spatial independence of flow velocity at intermediate and long distances documents the deposition and subsequent erosion of bars in a random manner, resulting in the spatial independence of flow velocity.

Channel Belt 1 is interpreted to document perennial deposits as the facies are predominantly low flow regime associated facies (e.g. facies F3, F4, F5) and do not vary within the channel belt. Therefore, we infer the intermediate-range transience in flow velocity is the result of periods of high and low flow velocity as the channel belt laterally migrated.

We interpret the short-range positive autocorrelation, intermediate-range negative autocorrelation, facies, and bar migration orientation in Channel Belts 3 and 4 to record short term stasis in flow velocity along with long term transience in flow velocity. Furthermore, using facies proportions, we interpret Channel Belt 3 to document ephemeral deposits as the facies record high flow regime (e.g. facies F8, F9, F10) and vary significantly within the channel belt. In Channel Belt 3, we interpret the intermediate-range transience of flow velocity is due to decreasing flow depth related to rapid filling of the channel belt. A majority of facies in Channel Belt 3 (e.g. Facies F9 and F10) are characteristic of high deposition rates that are common in ephemeral deposits, and support the hypothesis of a rapidly filling channel belt (Figure 5c).

Channel Belt 4 is interpreted to document perennial deposits as the facies are predominantly low flow regime associated facies (e.g. facies F3, F4, F5) and have little variability within the channel belt. Therefore, we infer the intermediate and long-range transience in flow velocity is due to alternating periods of high and low flow velocity rather than rapid infilling of the channel belt.

We interpret Channel Belt 2 documents perennial deposits; the majority of the facies are diagnostic of lower flow regime conditions which are interpreted by North and Taylor (1996) to record low discharge and low flow velocity conditions (Figure 5b). Facies in Channel Belt 4 document both high and low flow conditions, but is primarily facies that are interpreted to document low flow regime (Figure 5e). Additionally, the short-range persistence and intermediate range transience of flow velocities document periods of alternating high and low flow. Therefore, we interpret this channel belt to be a combination of perennial and ephemeral flow conditions.

DISCUSSION

The paleoflow velocities and associated error is minimized by minimizing the error in the paleoslope calculation. When we constrain the slope error, we minimize the variance in flow estimates by over half. However, the same variables that contribute to the error in the slope estimate are also used in the velocity calculation, so minimizing error in the field measurements has a two-fold effect of constraining slope, and velocity calculations. Further work is needed to compare measured velocity data from modern systems and the calculated slope and velocity from grain size and flow depth. However, we note that Moran's *I* values are rather insensitive to the variance in flow velocity in our Monte Carlo simulations and give us quantitative bounds for Moran's *I* for each bedset (Figure 4).

From the spatial autocorrelation results, we interpret the rate of lateral migration within laterally-accreting channel belts, to be proportional to preservation potential of the subjacent bars. Furthermore, we interpret that the rate of in channel belt aggradation within downstream-accreting channel belts is also proportional to the preservation potential of subjacent bars. Results from this study suggest intra-channel belt preservation of allogenic signals to be opposite those of basin-scale channel-belt stacking patterns documented by Straub and Esposito (2013). At the bar scale, if a channel moves laterally quickly the underlying basin-scale strata is removed, but the intra-channel belt architecture is preserved. Conversely, if a channel doesn't migrate laterally, the basin-scale channel-belt stacking pattern is better preserved. However, if downstream migrating bars aggrade quickly enough, both the basin-scale and intra-channel belt architecture is preserved. Therefore there is a scale-dependent tradeoff in signal preservation from intra-channel belt architecture to basin-scale stacking patterns. This concept provides insight into the scales that future studies should consider when attempting to resolve external signals. Systems with deep laterally-migrating channel belts should be considered ideal when attempting to resolve signals at the intra-channel belt scale, while systems with shallow downstream-migrating channel belts should be considered ideal to study when attempting to resolve basin-scale signals. Furthermore, the spatial relationships between some bedsets are non-random, and are related to both external controls and hydrologic conditions

CONCLUSION

We interpret perennial and ephemeral fluvial systems in the lower Wasatch Formation based on spatial dependence and facies types. Perennial rivers have short range positive autocorrelation, intermediate and long range negative autocorrelation, and are composed of low-flow regime bedforms. Ephemeral rivers have both short range positive autocorrelation, long range negative autocorrelation, and contain sedimentary structures and facies indicative of upper flow regime and high deposition rates. External signals that are completely masked by deposition and subsequent erosion are characterized by no spatial dependence at all but short distances. However, facies proportions and sedimentary structures document facies associated with both perennial and ephemeral rivers.

This article quantitatively documents a paleoflow velocity calculation method and the associated sources and propagation of error through the system of equations. Additionally we document perennial and ephemeral signals within fluvial channel belts. We use a workflow to calculate mean flow velocity and associated error for each bedset. Using Moran's *I*, facies patterns, and migration orientations, we document spatial dependence and independence in mean flow velocity. We interpret short and long-range spatial dependence and facies types to differentiate between rapid filling of ephemeral channel belts, and the fluctuations of flow velocity of perennial channel belts. Furthermore, we document that repeated deposition and erosion of barforms results in local spatial dependence, but intermediate and long-range independence of flow velocities. Concepts developed in this study provide context from a world class fluvial outcrop to previous tank and numerical studies on the preservation of external signals, and are applicable to both modern and ancient fluvial systems around the globe.

APPENDIX OF VARIABLES

ν	kinematic viscosity of water
ρ	density of water
τ_b	bed shear stress
C	constant equal to 1
C_d	drag coefficient
D_{90}	maximum grain size
$E(I)$	expected value of Moran's I
F	ratio of boundary stress to skin-friction shear stress
g	gravitational acceleration
H	flow depth
h_d	0.3 times flow depth
h_d/λ	dune height-to-length ratio
κ	von Kármán's constant
N	number of bedsets
R	specific gravity of a particle in water
S	slope

u_* shear velocity

$w_{s(Dmaxs)}$ settling velocity of coarsest grain in suspension

W_{ij} spatial weights

$\bar{y}$ global mean flow velocity

y_i *i*-th observation in Moran's *I*

y_j *j*-th observation in Moran's *I*

z_0 height above the bed at which the velocity goes to zero

z height of the velocity measurement,

ACKNOWLEDGEMENTS

This article benefited from early constructive reviews by Kyle Straub, Brady Foreman, an anonymous reviewer, _____________ and __________. Financial support was provided by the Chevron Center of Research Excellence (Colorado School of Mines), AAPG Student Grant-in-aid, Rocky Mountain Section of SEPM Fluvial Sedimentology Award, Rocky Mountain Association of Geologists Scholarship, Devon Energy Scholarship, and the Hemmesch and Burch Fellowships from the Colorado School of Mines. We thank Duncan Metcalfe, Corinne Springer, Dave Potter, and the Natural History Museum of Utah for field support and access to Desolation Canyon.

REFERENCES CITED

Allen, J. P., Fielding, C. R., Gibling, M. R., & Rygel, M. C. (2014). Recognizing products of palaeoclimate fluctuation in the fluvial stratigraphic record: An example from the Pennsylvanian to Lower Permian of Cape Breton Island, Nova Scotia. *Sedimentology*, *61*(5), 1332–1381.

Allen, J. P., Fielding, C. R., Rygel, M. C., & Gibling, M. R. (2013). Deconvolving signals of tectonic and climatic controls from continental basins: an example from the late Paleozoic Cumberland Basin, Atlantic Canada. *Journal of Sedimentary Research*, *83*(10), 847–872.

Fielding, C. R., Allen, J. P., Alexander, J., & Gibling, M. R. (2009). Facies model for fluvial systems in the seasonal tropics and subtropics. *Geology*, *37*(7), 623–626.

Ford, G. L., & Pyles, D. R. (2014). A hierarchical approach for evaluating fluvial systems: Architectural analysis and sequential evolution of the high net-sand content, middle Wasatch Formation, Uinta Basin, UtahGeohorizon. *AAPG Bulletin*, *98*(7), 1273–1304.

Foreman, B. Z., Heller, P. L., & Clementz, M. T. (2012). Fluvial response to abrupt global warming at the Palaeocene/Eocene boundary. *Nature*, *491*(7422), 92.

Herman, J., & Usher, W. (2017). SALib: an open-source Python library for sensitivity analysis. *The Journal of Open Source Software*, *2*(9).

Hunter, J. D. (2007). Matplotlib: A 2D graphics environment. *Computing in Science & Engineering*, *9*(3), 90–95.

Jerolmack, D. J., & Paola, C. (2010). Shredding of environmental signals by sediment transport. *Geophysical Research Letters*, *37*(19).

Keighley, D., Flint, S., Howell, J., Andersson, D., Collins, S., Moscariello, A., & Stone, G. (2002). Surface and Subsurface Correlation of the Green River Formation in Central Nine Mile Canyon, SW Uinta Basin, Carbon and Duchesne Counties, East-Central Utah (MP-02-1).

Leopold, L. B., & Wolman, M. G. (n.d.). Miller] P. 1964. Fluvial processes in geomorphology. *San Francisco, California, Freeman*, *522*, 135–163.

Lynds, R. M., Mohrig, D., Hajek, E. A., & Heller, P. L. (2014). Paleoslope reconstruction in sandy suspended-load-dominant rivers. *Journal of Sedimentary Research*, *84*(10), 825–836.

McKee, E., Crosby, E. t, & Berryhill Jr, H. (1967). Flood deposits, Bijou Creek, Colorado, June 1965. *Journal of Sedimentary Research*, *37*(3).

McKinney, W. (2010). Data structures for statistical computing in python (Vol. 445, pp. 51–56). Presented at the Proceedings of the 9th Python in Science Conference, Austin, TX.

Meinzer, O. E. (1923). Outline of ground-water hydrology. *US Geological Survey Water Supply Paper*, *494*, 5.

Moran, P. A. (1950). Notes on continuous stochastic phenomena. *Biometrika*, *37*(1/2), 17–23.

North, C. P., & Taylor, K. S. (1996). Ephemeral-fluvial deposits: integrated outcrop and simulation studies reveal complexity. *AAPG Bulletin*, *80*(6), 811–830.

Oliphant, T. E. (2006). *A guide to NumPy* (Vol. 1). Trelgol Publishing USA.

Osmond, J. C. (1964). Tectonic history of the Uinta basin, Utah.

Pérez, F., & Granger, B. E. (2007). IPython: a system for interactive scientific computing. *Computing in Science & Engineering*, *9*(3).

Picard, M. D. (1956). Summary of Tertiary oil and gas fields in Utah and Colorado. *AAPG Bulletin*, *40*(12), 2956–2960.

Pisel, J. R., Pyles, D. R., & Kirschbaum, M. A. (2018). The influence of lateral topographic confinement on fluvial channel-belt clustering, compensation and connectivity–lower Wasatch Formation and Dakota Sandstone, Utah, USA. *Sedimentology*, *65*(2), 597–619.

Prokoph, A., & Agterberg, F. P. (1999). Detection of sedimentary cyclicity and stratigraphic completeness by wavelet analysis: an application to late Albian cyclostratigraphy of the

Western Canada sedimentary basin. *Journal of Sedimentary Research*, *69*(4).

Prokoph, A., & El Bilali, H. (2008). Cross-wavelet analysis: a tool for detection of relationships between paleoclimate proxy records. *Mathematical Geosciences*, *40*(5), 575–586.

Saltelli, A. (2002). Making best use of model evaluations to compute sensitivity indices. *Computer Physics Communications*, *145*(2), 280–297.

Saltelli, A., Annoni, P., Azzini, I., Campolongo, F., Ratto, M., & Tarantola, S. (2010). Variance based sensitivity analysis of model output. Design and estimator for the total sensitivity index. *Computer Physics Communications*, *181*(2), 259–270.

Sewall, J. O., & Sloan, L. C. (2006). Come a little bit closer: A high-resolution climate study of the early Paleogene Laramide foreland. *Geology*, *34*(2), 81–84.

Shields, A. (1936). Application of similarity mechanics and turbulence research on shear flow. *Mitteilungen Der Preußischen Versuchsanstalt Für Wasserbau (in German)*, (26).

Sobol, I. M. (2001). Global sensitivity indices for nonlinear mathematical models and their Monte Carlo estimates. *Mathematics and Computers in Simulation*, *55*(1–3), 271–280.

Trampush, S., Huzurbazar, S., & McElroy, B. (2014). Empirical assessment of theory for bankfull characteristics of alluvial channels. *Water Resources Research*, *50*(12), 9211–9220.

Von Kármán, T. (1931). Mechanical similitude and turbulence.

Wiberg, P. L., & Rubin, D. M. (1989). Bed roughness produced by saltating sediment. *Journal of Geophysical Research: Oceans*, *94*(C4), 5011–5016.

FIGURE CAPTIONS

Figure 1. (A) Map showing the location of the Uinta Basin and bounding structures. Inset is a chronostratigraphic chart of the Uinta Basin. The lower Wasatch Formation lies between the

Flagstaff Limestone and middle Wasatch Formation and is the focus of this study. (B) Photopanel of the field area showing the locations of the 274 channel belts. The five used in this study are labeled 1-5 and are highlighted by the colored boxes.

Figure 2. Stratigraphic cross sections through the five channel belts within the lower Wasatch Formation used in this study. Sediment transport is into the page for all channel belts. Bedsets are colored according to the dominant facies within the bedset. Brown and green colors reflect facies with clay-sized sediment, while yellow and orange are facies with silt and sand. Facies proportions by area are documented in the pie charts next to each channel belt.

Figure 3. (A) Grain-size distributions for the channel belts used in this study. Grain-size measurements were made throughout the measured sections, and across the outcrop face. (B) Box and whisker plots of mean flow velocities calculated for bedsets in channel belts. (C) Box and whisker plots of flow depths measured from bar-form thicknesses within the channel belts.

Figure 4. Two-dimensional kernel density estimate plot of flow velocity and flow depth for all Monte Carlo simulations. Darker colors are areas with fewer points and lighter colors have higher density of points. The velocity and flow depth for each bedset in the five documented channel belts in the lower Wasatch Formation are plotted above to visualize alignment of the variance with the mean values.

Figure 5. (A)Spatially lagged Moran’s *I* values for channel belts in the lower Wasatch Formation. Increasing the neighborhood structure to include bedsets not directly in contact with

one another documents both short and long-range changes in spatial dependence. (B-F) Spatially lagged Moran's *I* values for all documented channel belts in the lower Wasatch Formation with boxplots documenting the variance of Moran's *I* due to variance in flow velocity calculations caused by error propagation from field measurements.

Table 1. Comparison of variance in mean flow velocity with and without variance in slope for each channel belt. When variance in slope is removed from the error propagation, the standard deviation of flow velocity is cut in roughly half.

Figure 1.

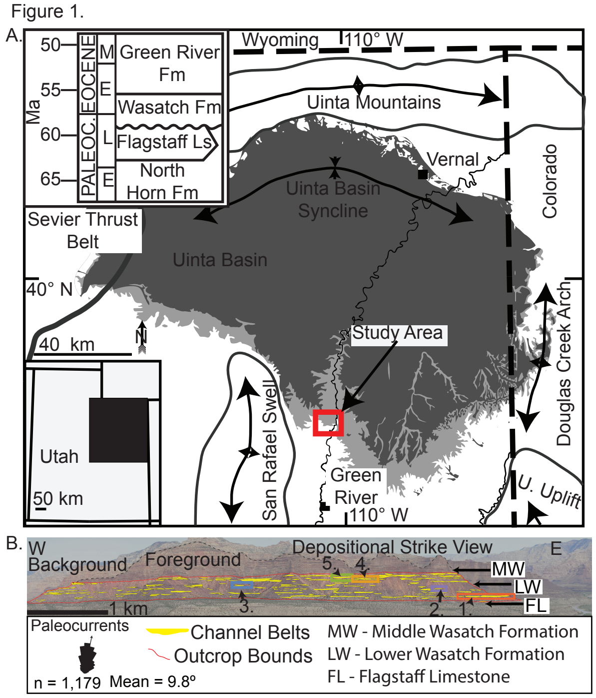
A.
Wyoming
110° W
50
55
60
65
Ma
PALEOC.
EOCENE
M
E
L
E
Green River Fm
Wasatch Fm
Flagstaff Ls
North Horn Fm
Uinta Mountains
Vernal
Uinta Basin Syncline
Colorado
Sevier Thrust Belt
Uinta Basin
40° N
40 km
N
Study Area
Douglas Creek Arch
Utah
50 km
San Rafael Swell
Green River
110° W
U. Uplift
B.
W
E
Background
Foreground
Depositional Strike View
5.
4.
MW
LW
FL
3.
2.
1.
1 km
Paleocurrents
n = 1,179 Mean = 9.8°
Channel Belts
Outcrop Bounds
MW - Middle Wasatch Formation
LW - Lower Wasatch Formation
FL - Flagstaff Limestone

Figure 2.

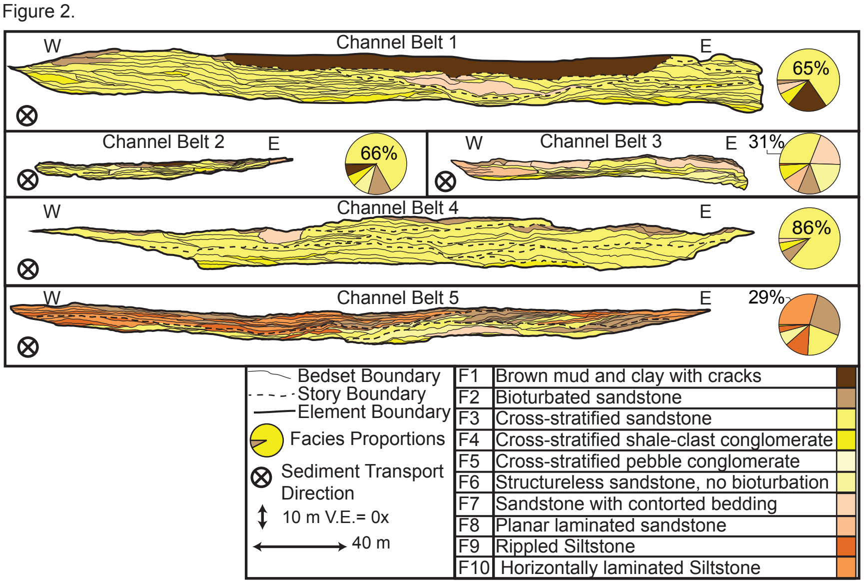
Channel Belt 1
W
E
65%
Channel Belt 2
E
66%
Channel Belt 3
W
E
31%
Channel Belt 4
W
E
86%
Channel Belt 5
W
E
29%
Bedset Boundary
Story Boundary
Element Boundary
Facies Proportions
Sediment Transport Direction
10 m V.E.= 0x
40 m
F1 Brown mud and clay with cracks
F2 Bioturbated sandstone
F3 Cross-stratified sandstone
F4 Cross-stratified shale-clast conglomerate
F5 Cross-stratified pebble conglomerate
F6 Structureless sandstone, no bioturbation
F7 Sandstone with contorted bedding
F8 Planar laminated sandstone
F9 Rippled Siltstone
F10 Horizontally laminated Siltstone

Figure 3.

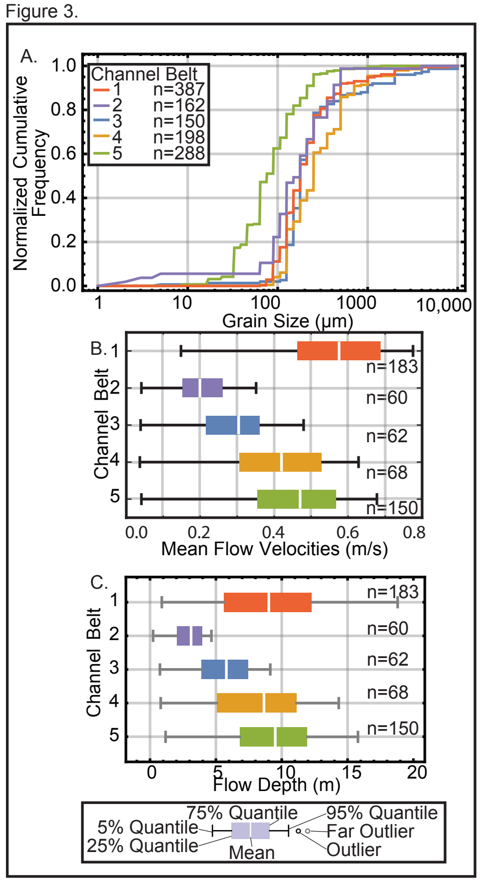

A.
Channel Belt
1 n=387
2 n=162
3 n=150
4 n=198
5 n=288
Normalized Cumulative Frequency
Grain Size (µm)
B.
Channel Belt
Mean Flow Velocities (m/s)
n=183
n=60
n=62
n=68
n=150
C.
Channel Belt
Flow Depth (m)
5% Quantile
25% Quantile
75% Quantile
Mean
95% Quantile
Far Outlier
Outlier

Figure 4.

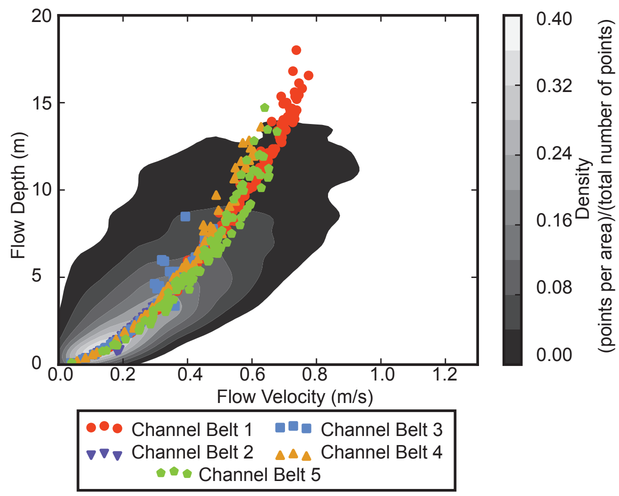

Flow Depth (m)
Flow Velocity (m/s)
0
5
10
15
20
0.0
0.2
0.4
0.6
0.8
1.0
1.2
0.40
0.32
0.24
0.16
0.08
0.00
Density
(points per area)/(total number of points)
Channel Belt 1
Channel Belt 2
Channel Belt 3
Channel Belt 4
Channel Belt 5

Figure 5.

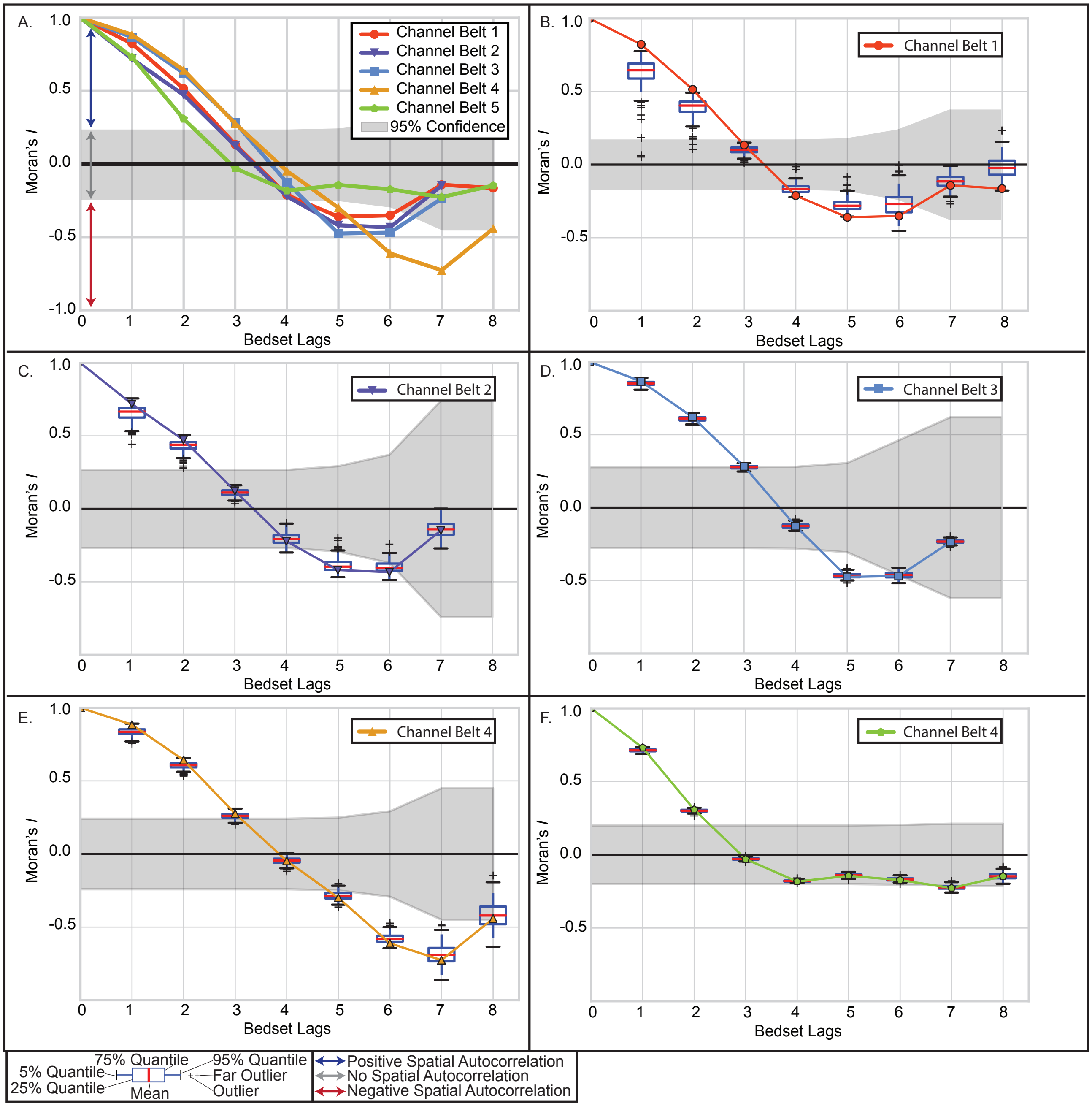
A.
B.
C.
D.
E.
F.
Channel Belt 1
Channel Belt 2
Channel Belt 3
Channel Belt 4
Channel Belt 5
95% Confidence
Moran's I
Bedset Lags
1.0
0.5
0.0
-0.5
-1.0
0
1
2
3
4
5
6
7
8
5% Quantile
25% Quantile
75% Quantile
Mean
95% Quantile
Far Outlier
Outlier
Positive Spatial Autocorrelation
No Spatial Autocorrelation
Negative Spatial Autocorrelation

Table 1.

Channel Belt	Mean Flow Velocity with Slope Variance (m/s)	Mean Flow Velocity Standard Deviation with Slope Variance (m/s)	Mean Flow Velocity without Slope Variance (m/s)	Mean Flow Velocity Standard Deviation without Slope Variance (m/s)
1	0.55	0.29	0.55	0.13
2	0.2	0.11	0.2	0.045
3	0.28	0.14	0.28	0.06
4	0.4	0.21	0.4	0.09
5	0.45	0.11	0.45	0.09